Heliogyro Orbital Control Authority

Heiligers, Jeannette; Guerrant, D.; Lawrence, D

Publication date
2015

Document Version
Accepted author manuscript

Published in
Proceedings of the 25th International Symposium on Space Flight Dynamics

HELIOGYRO ORBITAL CONTROL AUTHORITY

Jeannette Heiligers(1), **Daniel Guerrant**(2), **Dale Lawrence**(2)

(1) *Delft University of Technology, Kluyverweg 1, 2629 HS Delft, the Netherlands*[1]

(2) *University of Colorado, Boulder, CO 80309, USA*

Abstract: *Solar sailing is an elegant form of space propulsion that reflects solar photons to produce thrust. Different sail configurations exist, including a traditional flat sail (either square- or disc-shaped) and a heliogyro, which divides the sail membrane into a number of long, slender blades, analogous to a helicopter rotor. The magnitude and direction of the induced thrust force depends on the sail's attitude with respect to the Sun, i.e. on the cone angle. At each cone angle, a flat sail can only generate force of particular magnitude and direction, while this paper demonstrates that a heliogyro can arbitrarily reduce the magnitude of the thrust vector through the additional control of pitching the blades. This gives the heliogyro more force control authority, which is exploited in this paper for orbital control. A linear-quadratic regulator feedback controller is used to quantify the maximum error in the injection state vector of a solar sail Sun-Earth sub-L_1 halo orbit from which the nominal orbit can still be recovered. The conclusion is that approximately an order of magnitude larger error in position and velocity can be accommodated, demonstrating superior capabilities of the heliogyro over a flat sail for orbital control.*

Keywords: *heliogyro, solar sail, sub-L_1 halo orbit, orbital control*

1. Introduction

Solar sailing is a relatively new form of spacecraft propulsion that exploits solar radiation pressure by using a large, very thin and highly reflective membrane to reflect solar photons, thereby inducing thrust. As a propellant-less form of propulsion, it has great potential for high-energy and long-duration missions and has recently been successfully demonstrated in space with the IKAROS [1], NanoSail-D2 [2] and LightSail-1 missions[2]. Each of these three missions employed a flat, square-shaped solar sail. However, renewed interest exists in the heliogyro concept [3]. This solar sail concept divides the sail area into a number of long, slender blades which are deployed from a central hub and maintained in a flat state

[1] Part of this work was performed as Research Associate at the Advanced Space Concepts Laboratory, Department of Mechanical and Aerospace Engineering, University of Strathclyde, Glasgow, G1 1XJ, United Kingdom, jeannette.heiligers@strath.ac.uk

[2] LightSail | The Planetary Society, http://sail.planetary.org/, accessed 20 June 2015

through spin-induced tension [4]. Not only does this allow simple packaging and deployment, it also removes the need for a relatively heavy mechanical deployment and stiffening structure as required for the flat sail configuration. The heliogyro concept is therefore more efficient, allowing greater thrust accelerations for the same sail loading (the spacecraft mass to sail area ratio).

Significant research has been conducted regarding the heliogyro's blade dynamics, stability and control [5] and its attitude control moment authority [6], but much remains to be explored in its orbital dynamics and control capabilities. Even its force-generating capabilities appear to hide some interesting possibilities. For example, the force vector with respect to the sun line that a flat sail can achieve is constrained to the surface of a so-called "force bubble"; however, this is not the case for a heliogyro. This paper shows that the heliogyro's additional ability of pitching its blades enables it to scale down the force magnitude in any direction. The heliogyro can therefore "fill up" the force bubble, allowing finer force control, which is exploited in this paper for orbital control. In particular, the ability of a flat sail and a heliogyro to correct for orbit injection errors into a solar sail Sun-Earth L_1 halo orbit are investigated and compared.

A solar sail sub-L_1 halo orbit has been proposed for several mission concepts (e.g. Geostorm [7] and Sunjammer [8]), and is one of the key missions enabled by solar sail technology [9]. By exploiting a solar sail, this mission concept efficiently positions a platform along the Sun-Earth line, sunward of the L_1 point. From such a vantage point, the platform can almost double the warning time for solar storms over existing infrastructure at L_1 (e.g. SOHO (ESA/NASA, 1996), ACE (NASA, 1997), WIND (NASA, 2004) and DSCOVR (NOAA/NASA, 2015)). This increased warning time is essential to allow operators of ground and space assets enough time to take appropriate action for incoming solar storms. While this mission concept has been investigated quite extensively (e.g. [7-9]), operational aspects such as recovery from injection errors have not been considered in great detail. In particular, a study to investigate the difference in performance between a flat sail and heliogyro in this respect has so far not been conducted.

To that end, this paper is structured as follows. First, Section 2 explains the heliogyro force model, supported by a detailed explanation of the reference frames and their transformations in Appendix A. Section 3 outlines a range of possible pitch profiles of the heliogyro's blades, followed by the impact of these pitch profiles on the heliogyro's force generating capabilities in Section 4. Section 5 derives and presents the solar sail halo orbits that will serve as a test case throughout this paper, followed by the design of a linear-quadratic regulator (LQR) to maintain these orbits under injection errors in Section 6. Finally, Section 7 presents the results, while Section 8 investigates sensitivity analyses on the error tolerance and the injection location along the orbit.

2. Heliogyro force model

This paper assumes an ideal solar sail model [4], which considers the sail to be perfectly reflecting and perfectly flat, without wrinkles or optical imperfections. Under these assumptions, the incoming solar photons are specularly reflected. The solar radiation pressure force and acceleration then act perpendicular to the sail surface (or the i^{th} heliogyro blade) and can be obtained through [10]

$$\mathbf{a}_{i,L_i} = 2P\frac{A_i}{m}\cos^2\alpha_i\hat{\mathbf{n}}_{L_i} \tag{1}$$

where P is the solar radiation pressure (4.563×10^{-6} N/m^2 at 1 Astronomical Unit (AU)) and A_i is the i^{th} blade area. The i^{th} blade's cone angle, α_i, is the angle between the Sun direction and the i^{th} blade's normal, $\hat{\mathbf{n}}_{L_i}$. To compute this angle, both vectors need to be defined in the same reference frame. This work considers four different reference frames ($S\left(\hat{\mathbf{s}},\hat{\mathbf{l}},\hat{\mathbf{p}}\right)$, $D\left(\hat{\mathbf{d}}_1,\hat{\mathbf{d}}_2,\hat{\mathbf{d}}_3\right)$, $B\left(\hat{\mathbf{b}}_1,\hat{\mathbf{b}}_2,\hat{\mathbf{b}}_3\right)$ and $L_i\left(\hat{\mathbf{x}},\hat{\mathbf{y}},\hat{\mathbf{z}}\right)$), which are detailed in Appendix A together with the transformations required to change between reference frames.

To compute the cone angle, first the Sun-direction is transformed from the Sun $S\left(\hat{\mathbf{s}},\hat{\mathbf{l}},\hat{\mathbf{p}}\right)$ reference frame, $\hat{\mathbf{s}}_S = \begin{bmatrix}1 & 0 & 0\end{bmatrix}^T$, into the i^{th} blade $L_i\left(\hat{\mathbf{x}},\hat{\mathbf{y}},\hat{\mathbf{z}}\right)$ reference frame:

$$\hat{\mathbf{s}}_{L_i} = \left[BL_i\right]^T\left[DB\right]^T\left[SD\right]^T\hat{\mathbf{s}}_S . \tag{2}$$

The blade's normal vector can be defined in the $L_i\left(\hat{\mathbf{x}},\hat{\mathbf{y}},\hat{\mathbf{z}}\right)$ frame as

$$\hat{\mathbf{n}}_{L_i} = \begin{bmatrix}0 & 0 & \text{sign}\left(\hat{\mathbf{s}}_{L_{i,3}}\right)\end{bmatrix}^T \tag{3}$$

where $\hat{\mathbf{s}}_{L_{i,3}}$ is the third component of the $\hat{\mathbf{s}}_{L_i}$ unit vector, and the sign function ensures the sail normal points away from the Sun direction. The blade's cone angle can then be computed from

$$\cos\alpha_i = \hat{\mathbf{s}}_{L_i}\cdot\hat{\mathbf{n}}_{L_i} . \tag{4}$$

To obtain the *total* solar radiation pressure acceleration on all N blades of the heliogyro in the $S\left(\hat{\mathbf{s}},\hat{\mathbf{l}},\hat{\mathbf{p}}\right)$, $D\left(\hat{\mathbf{d}}_1,\hat{\mathbf{d}}_2,\hat{\mathbf{d}}_3\right)$ or $B\left(\hat{\mathbf{b}}_1,\hat{\mathbf{b}}_2,\hat{\mathbf{b}}_3\right)$ reference frames, the individual $\mathbf{a}_{i,L_i}$ components need to be transformed to the respective frame and summed. For the Sun $S\left(\hat{\mathbf{s}},\hat{\mathbf{l}},\hat{\mathbf{p}}\right)$ reference frame this becomes:

$$\mathbf{a}_S = \sum_{i=1}^{N} [SD][DB][BL_i]\mathbf{a}_{i,L_i} \ . \tag{5}$$

Note that the total acceleration vector changes over each revolution and is therefore averaged over two revolutions. Also note that throughout this paper a value for the number of blades of $N = 4$ will be assumed.

The term $2PA_i / m$ in Eq. (1) is usually rewritten using the so-called characteristic acceleration, $a_{c,i}$. The characteristic acceleration is the acceleration that the sail or heliogyro blade can achieve when facing the Sun (i.e. $\alpha_i = 0$) at Earth's distance ($r_{AU} = 1$ AU).

$$a_{c,i} = \beta_i \frac{\mu}{r_{AU}^2}, \quad \beta = \sum_{i=1}^{N} \beta_i \tag{6}$$

with μ the gravitational parameter of the Sun and β the solar sail lightness number. At any other distance from the Sun, r, the solar sail acceleration becomes:

$$\mathbf{a}_{i,L_i} = \beta_i \frac{\mu}{r^2} \cos^2 \alpha_i \hat{\mathbf{n}}_{L_i} \ . \tag{7}$$

This paper assumes a baseline lightness number of $\beta = 0.0363$ based on the expected performance of relatively mature flat sail technology designed for the Sunjammer mission [8]. Note that, due to the reduced sail system mass, a near-term value for a similarly-mature heliogyro-type sail would be approximately $\beta = 0.08$ [3].

3. Heliogyro pitch profiles

Equation (7) provides the solar radiation pressure acceleration in the $L_i(\hat{\mathbf{x}}, \hat{\mathbf{y}}, \hat{\mathbf{z}})$ frame, which can easily be transformed into any of the other reference frames using Appendix A. However, the pitch angle of the blade, θ_i, is required to compute the $[BL_i]$ transformation matrix, which depends on the pitch profile selected. References 3 and 10 define three different pitch profiles, which can be used independently or in combination:

1. Collective profile ('co')
2. ½-Period cyclic profile (half-p, 'hp')
3. 1-Period cyclic profile (cyclic , 'cy')

Each of the pitch profiles and its effect on the solar radiation pressure force and moment is illustrated in Figure 1, which is taken from Reference 10. The 'co' profile pitches the blades collectively, while the 'hp'- and 'cy'-profiles pitch the blades cyclically or sinusoidally. The 'hp' profile repeats after two revolutions, while the 'cy' profile repeats after one revolution.

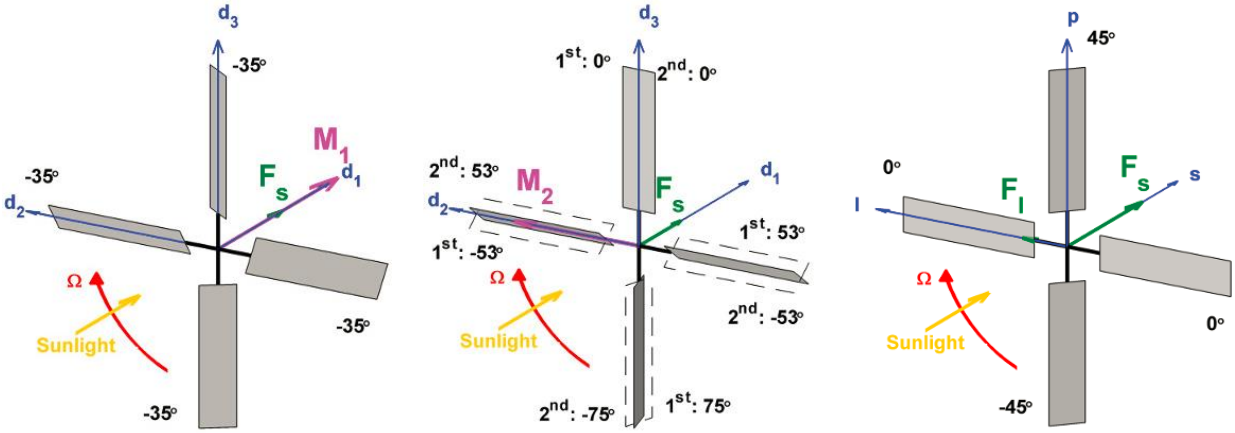

Figure 1 Illustration of pitch profiles at zero cone angle of the heliogyro (source: [10]).

Reference 10 provides the i^{th} blade's pitch angle for any combination of the three pitch profiles:

$$\theta_i = -a_{co} + a_{hp}\sin\left[\frac{1}{2}\left(\psi_i - \phi_{hp} - \text{sign}\left(a_{hp}\right)\frac{\pi}{2}\right)\right] + a_{cy}\sin\left(\psi_i - \phi_{cy}\right) \tag{8}$$

where a_{co}, a_{hp}, and a_{cy} are the amplitudes of the collective, half-p and cyclic profiles, respectively, and ϕ_{hp} and ϕ_{cy} are the phase angles of the half-p and cyclic profiles, respectively.

4. Heliogyro force capabilities

For a flat, non-spinning solar sail at 1 AU, pitched with respect to the Sun direction at a cone angle α (and a clock angle $\delta = 0$, see Figure 16a in Appendix A), the normal vector to the sail area can be written in the $S\left(\hat{\mathbf{s}},\hat{\mathbf{l}},\hat{\mathbf{p}}\right)$ reference frame as

$$\hat{\mathbf{n}}_S = \begin{bmatrix}\cos\alpha & \sin\alpha & 0\end{bmatrix}^T . \tag{9}$$

The solar radiation pressure force that such a flat sail can achieve at 1 AU, per square meter sail area, and in the direction along the Sun line, F_s, and perpendicular to it, F_l, can be obtained from Eq. (1). Considering an interval for the cone angle of $\alpha = \left[-90^o, 90^o\right]$, the result is a "bubble-shaped" force curve as shown in Figure 2.

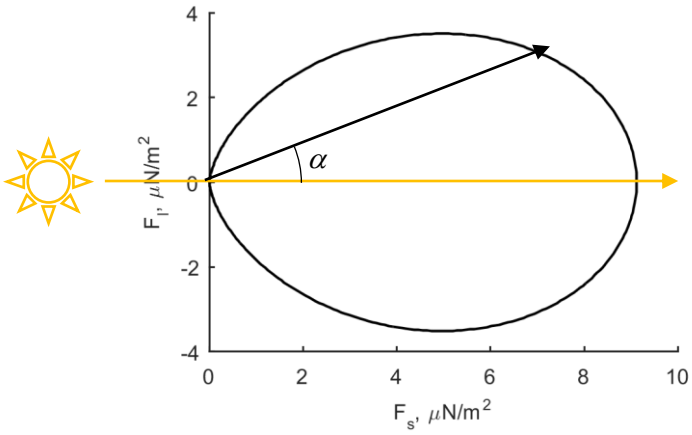

Figure 2 Flat solar sail "bubble-shaped" force curve providing the force per square meter sail area at 1 AU for α = [-90, 90] deg.

As the heliogyro has the additional control of pitching the blades (in a collective, cyclic, or half-p manner as described in Figure 1) the achievable (F_s, F_l)-combinations are not constrained to the edge of the bubble, but can instead take on any value within the bubble. This is demonstrated in Figure 3, which shows contours of equal pitch amplitudes for the collective, half-p and cyclic pitch profiles. Each curve represents one specific amplitude of one of the profiles and is constructed by again considering an interval for the heliogyro's cone angle of $\alpha = \left[-90^o, 90^o\right]$ and assuming $\delta = 0$. Note that the curves for negative values of the amplitudes can be obtained by mirroring the figures on the left hand side of Figure 3 in the (x, y)-plane.

The results in Figure 3 show that a heliogyro can be regarded as enabling a highly-variable lightness number, allowing it to scale the solar radiation pressure force between zero and that of an equivalent-area flat solar sail. Note that the half-p profile cannot generate *any* combination of the force magnitude and direction, as shown by the white region in the plot on the right hand side of Figure 3b. However, this white region can be captured by using a collective or cyclic profile, which *do* allow any combination of the force magnitude and direction. It is this property of a heliogyro, i.e. enabling a highly-variable lightness number, which is exploited in this paper for orbital control. In particular, to correct for injection errors into a solar sail Sun-Earth L_1 solar sail halo orbit.

a) **Collective profile**

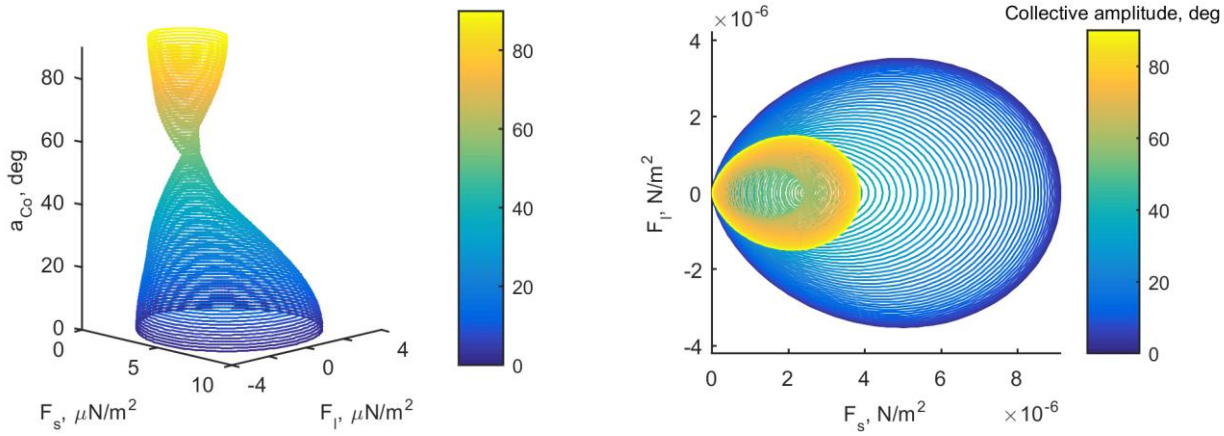

b) **Half-p profile,** $\phi_{hp} = -\frac{1}{2}\pi$

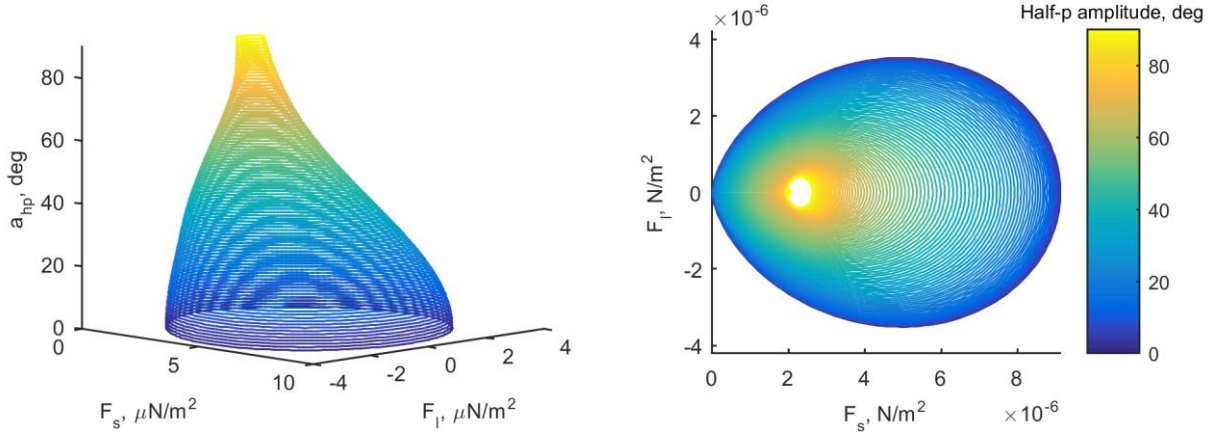

c) **Cyclic profile,** $\phi_{cy} = -\frac{1}{2}\pi$

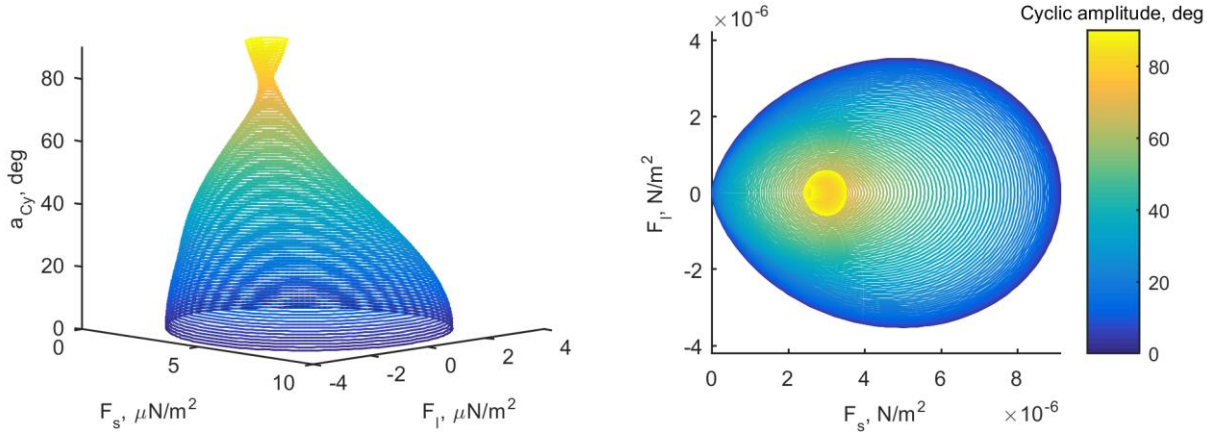

Figure 3 Heliogyro "bubble-shaped" force curves providing the force per square meter sail area at 1 AU for α = [-90, 90] deg and different pitch profiles.

5. Solar sail Sun-Earth L_1 halo orbits

As indicated in the introduction of this paper, one near-term application of solar sail technology is an advanced space weather forecasting platform at a sub-L_1 location [9]. By simply placing a Sun-facing sail on the Sun-Earth line, the L_1 point can be displaced sunward, to a sub-L_1 location. For a sail with Sunjammer's lightness number, this would enable an increase in the solar storm warning time by a factor of 1.6 compared to existing infrastructure at the L_1 point. In reality, the sail cannot be placed exactly *on* the Sun-Earth line as this causes solar radio interference during communications. It has therefore been suggested to place the sail in a solar sail halo orbit around the sub-L_1 point such that it orbits a 5 deg solar exclusion zone (SEZ) [11].

The generation of solar sail halo orbits has been investigated before (e.g. References 12-14), and the approach is briefly repeated here, starting with the solar sail dynamics in the Sun-Earth circular restricted three-body problem (CR3BP).

5.1 Solar sail Sun-Earth circular restricted three-body problem

The CR3BP describes the motion of an infinitely small mass, m, under the influence of the gravitational attraction of two much larger primary masses, m_1 and m_2. In the case of the solar sail Sun-Earth CR3BP, m represents the solar sail spacecraft and m_1 and m_2 are the Sun and Earth, respectively. The CR3BP further assumes that the gravitational influence of the small mass on the larger masses can be neglected and that the larger masses move in circular orbits about their common center-of-mass. Figure 4 shows the synodic reference frame employed in the CR3BP that rotates at a constant angular velocity, ω, about the z-axis, $\boldsymbol{\omega} = \omega\hat{\mathbf{z}}$.

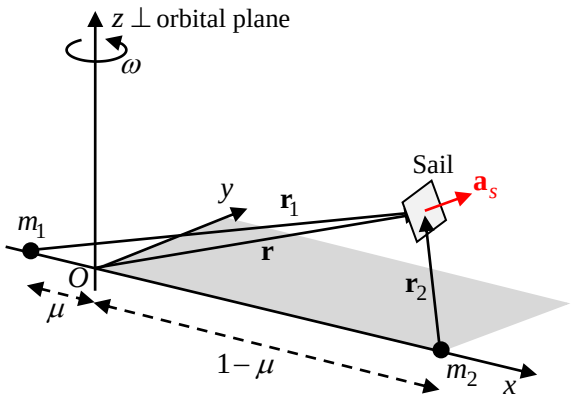

Figure 4 Schematic of solar sail circular restricted three-body problem.

The dynamics of the CR3BP are made dimensionless by taking the sum of the two larger masses as the unit of mass, i.e. $m_1 + m_2 = 1$, the distance between the main bodies as the unit of length, and $1/\omega$ as the unit of time (1 year is then represented by 2π). With the mass ratio $\mu = m_2 / (m_1 + m_2)$, the masses of the large bodies become $m_1 = 1 - \mu$ and $m_2 = \mu$, and their location along the x-axis become $-\mu$ and $1 - \mu$, respectively.

In this reference system, the motion of the solar sail is described by [4]:

$$\ddot{\mathbf{r}} + 2\boldsymbol{\omega} \times \dot{\mathbf{r}} + \boldsymbol{\omega} \times (\boldsymbol{\omega} \times \mathbf{r}) = \mathbf{a}_{\text{CR3BP}} - \nabla V \tag{10}$$

with $\mathbf{r} = \begin{bmatrix} x & y & z \end{bmatrix}^T$ the position vector of m, $\mathbf{a}_{\text{CR3BP}}$ the solar sail acceleration of Eq. (7) transformed to the CR3BP reference frame and V the gravitational potential. The latter two are given by

$$\mathbf{a}_{\text{CR3BP}} = \beta \frac{1-\mu}{r_1^2} \left(\hat{\mathbf{n}}_{\text{CR3BP}} \cdot \hat{\mathbf{r}}_1 \right)^2 \hat{\mathbf{n}}_{\text{CR3BP}} \tag{11}$$

$$V = -\left(\frac{1-\mu}{r_1} + \frac{\mu}{r_2} \right) \tag{12}$$

with $\hat{\mathbf{n}}_{\text{CR3BP}}$ the solar sail normal vector in the CR3BP reference frame, and the vectors $\mathbf{r}_1$ and $\mathbf{r}_2$ defined as $\mathbf{r}_1 = \begin{bmatrix} x + \mu & y & z \end{bmatrix}^T$ and $\mathbf{r}_2 = \begin{bmatrix} x - (1-\mu) & y & z \end{bmatrix}^T$. Following Reference 4, the centripetal acceleration in Eq. (10) can be written as the gradient of a scalar potential function and combined with the gravitational potential into a new, effective potential, $U = -\left(x^2 + y^2 \right)/2 - \left((1-\mu)/r_1 + \mu/r_2 \right)$. The solar sail dynamics in the CR3BP are then described by:

$$\ddot{\mathbf{r}} + 2\boldsymbol{\omega} \times \dot{\mathbf{r}} = \mathbf{a}_{\text{CR3BP}} - \nabla U \,. \tag{13}$$

5.2 Solar sail halo orbits

Many works in the literature (e.g., [12-17]) describe methods to find solar sail periodic (halo) orbits under the dynamics described in Eq. (13) or similar systems. In this paper, the same approach as in Reference 14 is adopted, which shows that solar sail halo orbits exist under different sail steering laws, e.g. $\hat{\mathbf{n}}_{\text{CR3BP}} = \hat{\mathbf{r}}_1$ and $\hat{\mathbf{n}}_{\text{CR3BP}} = \begin{bmatrix} 1 & 0 & 0 \end{bmatrix}^T$. In this work, the latter steering law is adopted.

A first guess for the orbits is obtained by approximating the equations of motion in Eq. (13) in the neighborhood of the sub-L_1 point by linearization and expanding the effective potential and solar sail acceleration terms to third order with a Taylor series. The Lindstedt-Poincaré method is subsequently used to find the third order solution to this approximated dynamical system. Details on the method can be

found in Reference 14. As these solutions only hold in the linearized system, the orbit quickly diverges when it is integrated in the full non-linear system of Eq. (13). A differential correction scheme is therefore applied to correct the initial conditions of the approximated orbit to find solar sail halo orbits in the full non-linear system. First, solar sail halo orbits with small amplitudes, i.e. close to the sub-L_1 point, are generated. A continuation scheme is subsequently applied to gradually increase the orbit's amplitude until the orbit fits around the 5 deg SEZ.

The resulting solar sail halo orbits are presented in Figure 5a-b for a range of sail lightness numbers, while Figure 5c-d provides the orbit for Sunjammer's performance, i.e. $\beta = 0.0363$. The initial conditions of the latter orbit are

$$\mathbf{x}_0 = \begin{bmatrix} \mathbf{r}_0 & \dot{\mathbf{r}}_0 \end{bmatrix}^T = \begin{bmatrix} 0.97971178 & 0 & 0.00296954 & 0 & 0.01322934 & 0 \end{bmatrix}^T, \tag{14}$$

which correspond to the most northern (i.e. out-of-ecliptic) location of a solar sail halo orbit with in- and out-of-plane amplitudes of 1,473,872 and 444,236 km, respectively.

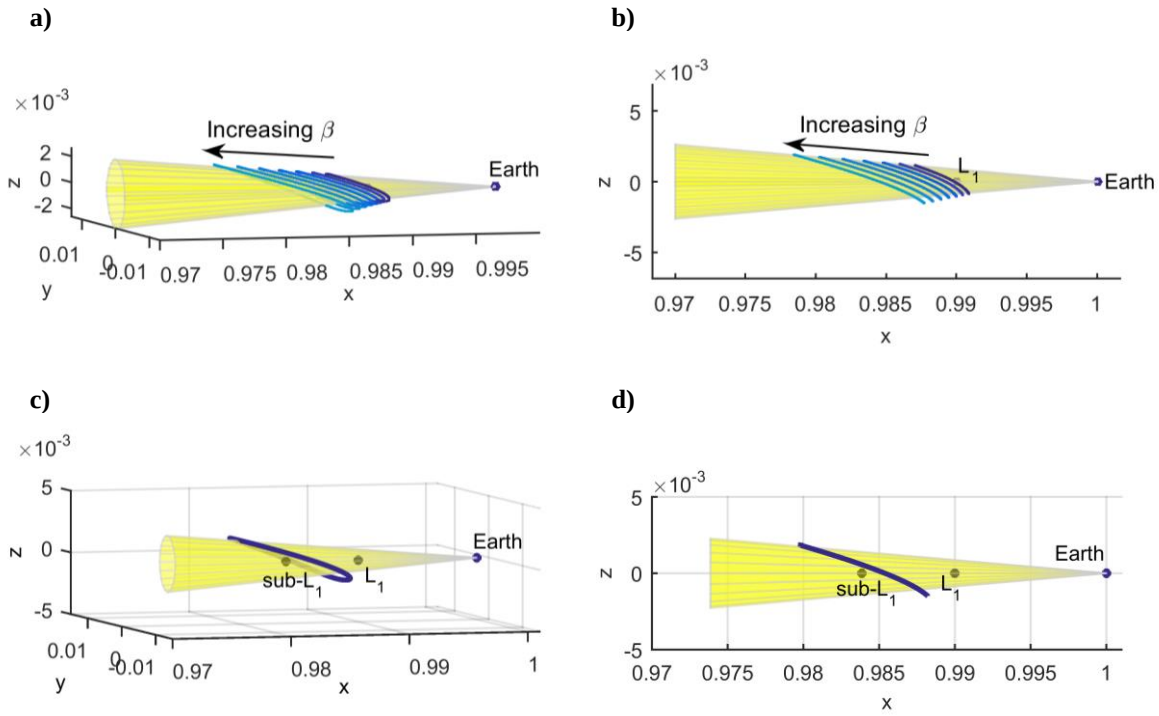

Figure 5 Solar sail halo orbits fitting around a 5 deg solar exclusion zone.
a-b) β = 0.01 - 0.04 . c-d) β = 0.0363.

6. Linear-quadratic controller

To investigate the orbital control capabilities of a heliogyro, this paper investigates how well the heliogyro can recover from errors on the injection into the solar sail halo orbits obtained in the previous section. To this end, an LQR feedback controller algorithm has been implemented in MATLAB/Simulink®, similar to the works in [18-20], which have demonstrated the applicability of this type of controller for similar problems. A simplified block diagram of the LQR is provided in Figure 6.

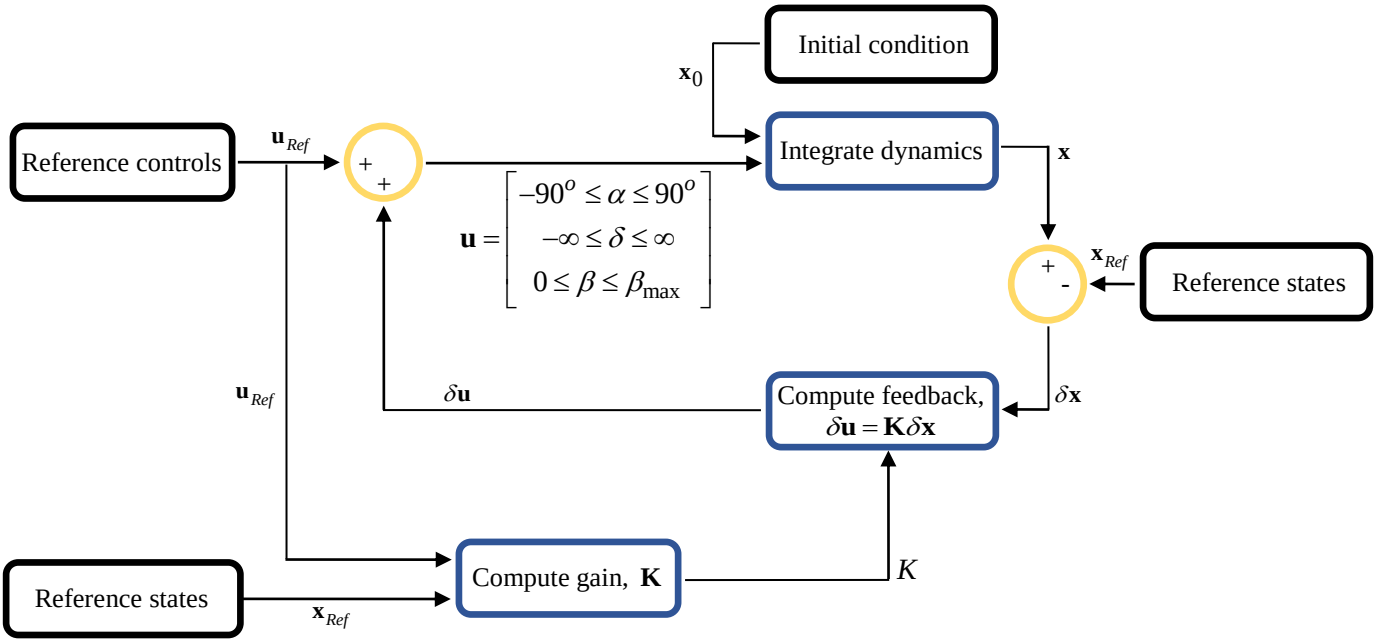

Figure 6 Simplified block diagram of LQR for solar sail halo orbit control. The constraint on the lightness number, $0 \le \beta \le \beta_{max}$, only applies to the heliogyro, not to the flat sail configuration.

As a result of the injection error, the trajectory, $\mathbf{x}$, will deviate from the nominal solar sail halo orbit, i.e. the reference trajectory, $\mathbf{x}_{Ref}$. The error on the state, $\delta\mathbf{x} = \mathbf{x} - \mathbf{x}_{Ref}$ is used to compute the required feedback control, $\delta\mathbf{u}$, which is added to the reference control to obtain the total control, $\mathbf{u} = \mathbf{u}_{Ref} + \delta\mathbf{u}$. The idea is that this total control will bring the trajectory back to the reference trajectory after some time.

For comparison, the solar sail halo orbits will be controlled both with a flat sail and a heliogyro. For a flat sail, the control components only include the sail's attitude. This attitude is described using the cone and clock angles (see Figure 16a of Appendix A), resulting in $\mathbf{u}(t) = \begin{bmatrix} \alpha(t) & \delta(t) \end{bmatrix}^T$. Note that the reference control consists of the cone and clock angles required to achieve $\hat{\mathbf{n}}_{\text{CR3BP}} = \begin{bmatrix} 1 & 0 & 0 \end{bmatrix}^T$ along the solar sail

halo orbit. Figure 7 shows an example of the reference controls for the solar sail halo orbit with $\beta = 0.0363$ of Figure 5c-d. For the heliogyro, the scalable lightness number is an additional control (i.e. $\mathbf{u}(t) = \left[\alpha(t) \quad \delta(t) \quad \beta(t)\right]^T$) to account both for the attitude of the heliogyro and the effect of pitching the blades. The block diagram in Figure 6 shows that the following bounds are enforced on these control components:

$$\begin{aligned} -90^o \le \alpha \le 90^o \\ -\infty \le \delta \le \infty \\ 0 \le \beta \le \beta_{\max} \quad \text{(for heliogyro)} \end{aligned} \tag{15}$$

If it is assumed that the state error is small, i.e. the sailcraft remains close to the reference trajectory at all time, the system dynamics can be described by linearizing the equations of motion in Eq. (13) around the reference conditions. For that, Eq. (13) is rewritten as a set of first order differential equations:

$$\dot{\mathbf{x}}(t) = \mathbf{f}\left(\mathbf{x}(t), \mathbf{u}(t), t\right) \tag{16}$$

to obtain

$$\delta\dot{\mathbf{x}} = \mathbf{A}\delta\mathbf{x} + \mathbf{B}\delta\mathbf{u} \tag{17}$$

with

$$\mathbf{A}_{6x6} = \left[\frac{\partial \mathbf{f}}{\partial \mathbf{x}}\right]_{\mathbf{x}_{Ref}, \mathbf{u}_{Ref}}, \quad \mathbf{B}_{6x3} = \left[\frac{\partial \mathbf{f}}{\partial \mathbf{u}}\right]_{\mathbf{x}_{Ref}, \mathbf{u}_{Ref}}. \tag{18}$$

Note that the notation of the time dependency is omitted for brevity. For a continuous-time linear system as described in Eq. (16) and a cost function defined as

$$J = \int_0^\infty \left(\delta\mathbf{x}^T \mathbf{Q} \delta\mathbf{x} + \delta\mathbf{u}^T \mathbf{R} \delta\mathbf{u}\right) dt \tag{19}$$

the feedback control law that minimizes the value of the cost is

$$\delta\mathbf{u} = -\mathbf{K}\delta\mathbf{x}\,. \tag{20}$$

The first and second terms on the right hand side of Eq. (19) penalise the transient state error and control effort, respectively, where the weighing matrices $\mathbf{Q}_{6x6} = 10{,}000\mathbf{I}_{6x6}$ and $\mathbf{R}_{3x3} = \mathbf{I}_{3x3}$ are obtained by trial and error. In Eq. (20), $\mathbf{K}_{3x6}$ is the gain matrix. The gain matrix can be found by solving the Riccati equation, which, in this work, is done by supplying the Matlab® function *lqr.m* with the matrices $\mathbf{A}$, $\mathbf{B}$, $\mathbf{Q}$, and $\mathbf{R}$.

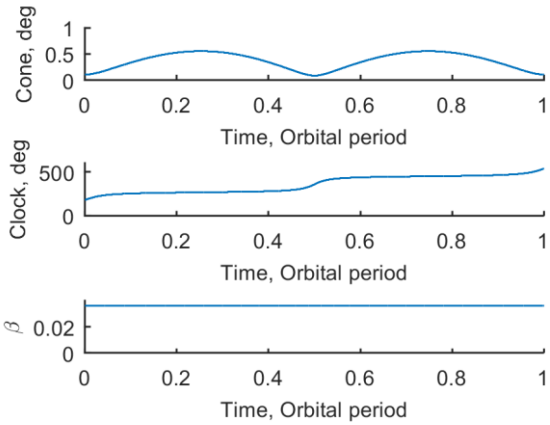

Figure 7 Reference control for solar sail halo orbit with β = 0.0363.

Finally, the injection error is modelled by perturbing the initial condition of the solar sail halo orbit, see Eq. (14), as

$$\mathbf{x}_0 = \begin{bmatrix} \mathbf{r}_0 + \Delta\mathbf{r}_0 & \dot{\mathbf{r}}_0 + \Delta\dot{\mathbf{r}}_0 \end{bmatrix}^T, \tag{21}$$

where the perturbation is provided in the direction of the unstable eigenvector, ξ (i.e. the eigenvector corresponding to the eigenvalue of the state transition matrix with $|\lambda_i| > 1$). With $\xi = \begin{bmatrix} \xi_p & \xi_v \end{bmatrix}^T$, the perturbations become $\Delta\mathbf{r}_0 = \Delta r_0 \xi_p$ and $\Delta\dot{\mathbf{r}}_0 = \Delta\dot{r}_0 \xi_v$. Section 7 will present results for a large range of perturbation magnitudes, Δr_0 and $\Delta\dot{r}_0$.

7. Results

This section provides the results of the LQR feedback controller of Section 6 to correct for errors in the injection of the solar sail halo orbits of Section 5. The control is considered successful if, after four orbital revolutions, the errors in position and velocity are smaller than a tolerance, ε. In this section a value of $\varepsilon = 0.0005$ (in CR3BP units) will be considered, which corresponds to a maximum allowable error of 75,000 km in position and 15 m/s in velocity. A sensitivity analysis on the magnitude of this tolerance is provided in Section 7.

The first results, in Figure 8, are for a lightness number equal to that of Sunjammer, i.e. $\beta = 0.0363$, see Figure 5c and d for the corresponding solar sail halo orbit. Figure 8a and b provide, respectively, the recoverable injection error for a flat solar sail and a heliogyro with an upper limit on the lightness number of 0.04, i.e. $\beta_{\max} = 0.04$. Both plots consider a wide range for the position and velocity error magnitudes

in the initial condition, but note the difference in scales between the plots; the heliogyro can correct for significantly larger injection errors in position and velocity than a flat sail, approximately an order of magnitude. Details for the case represented by the black "X" in Figure 8b are given in plots c and d, showing how the heliogyro settles the lightness number around the nominal value of 0.0363 and how the orbit is recovered.

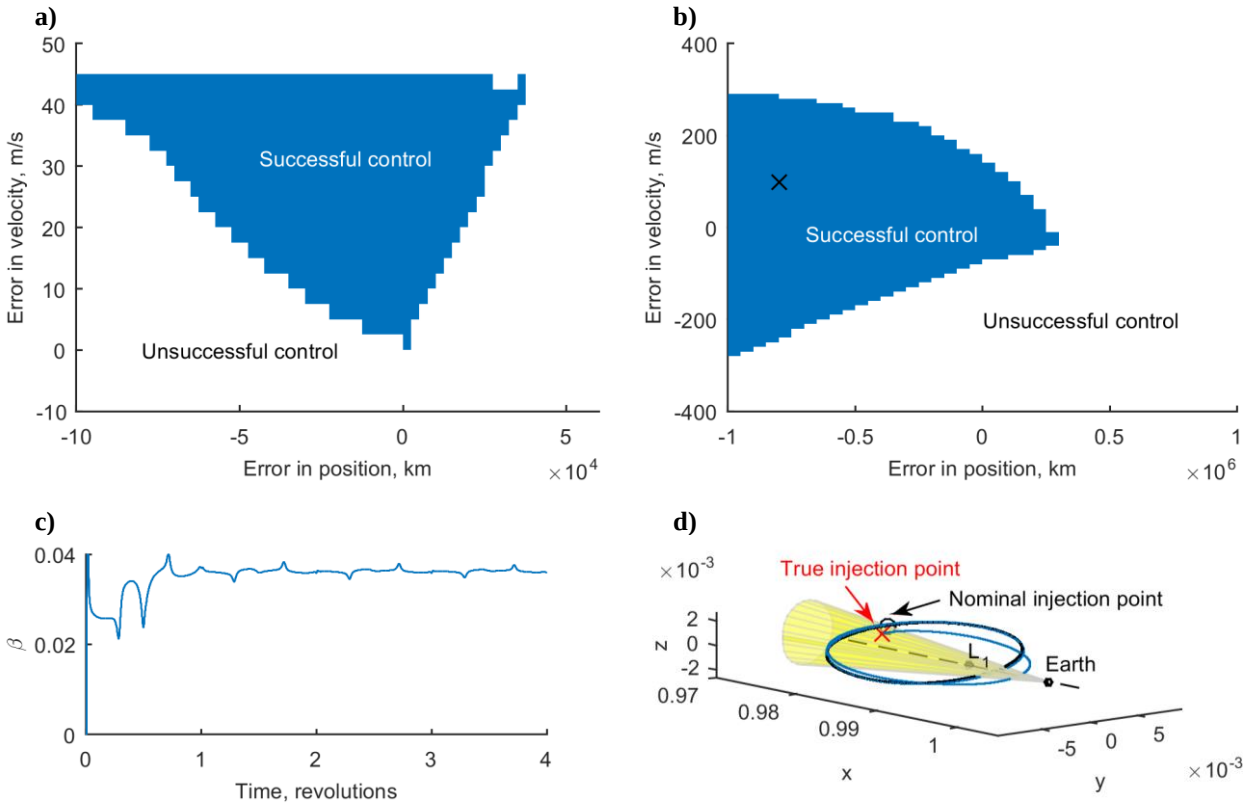

Figure 8 Orbital control of solar sail halo orbit with $\beta = 0.0363$. a-b) Recoverable injection error for (a) a flat sail and (b) heliogyro with $\beta_{max} = 0.04$. c-d) Detailed results for black marker in plot b).

Note that, although the upper limit on the lightness number of 0.04 is larger than Sunjammer's flat sail near-term technology, it is still a realistic value. As stated in the introduction, similar near-term heliogyro technology can enable lightness numbers of approximately $\beta = 0.08$. Also note that increasing the (constant) lightness number for the flat sail to 0.04 (while the solar sail halo orbit is designed for a value of 0.0363) leads to the situation that *no* injection error, no matter how small the error, can be recovered from. Only the heliogyro's unique ability to change the lightness number allows the use of a larger lightness number than required for the solar sail halo orbit, as it can reduce the lightness number and settle it around the nominal value once the injection error has been overcome.

To show the effect of other values for β_{max} on the recoverable injection error, Figure 9 has been included. As can be expected, the larger the value for β_{max}, the larger the injection error that can be corrected for. In fact, for a value of $\beta_{max} = 0.038$ the heliogyro enables an exact order of magnitude larger error in both position and velocity range compared to the flat sail. This is an increase in the nominal lightness number of 5 percent. Note that the small gap in the recoverable injection error surface for $\beta_{max} = 0.037$ is caused by the inability to satisfy the error tolerance on the position. More details on such gaps are provided in Section 8.2 where the sensitivity on the error tolerance is further investigated.

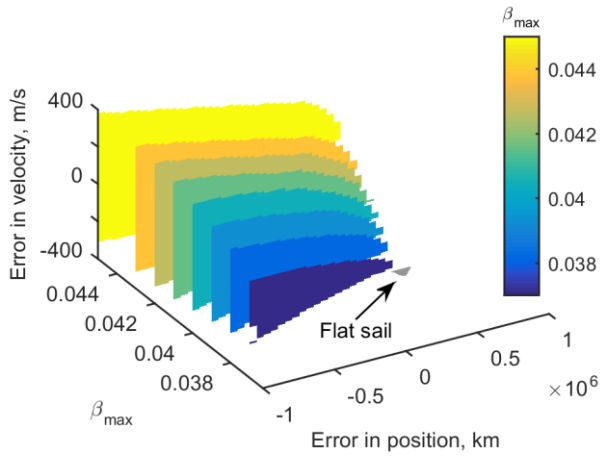

Figure 9 Orbital control of solar sail halo orbit with β = 0.0363. Recoverable injection error for flat sail (grey) and heliogyro with different values for β_{max} (color).

Figure 10 provides some additional details on the lightness number control profile for the case indicated by the black marker in Figure 8b for different values for β_{max}. The full profiles are shown in plot a with further details in plots b and c. The figure shows that the lightness number control profile is very similar for each value for β_{max} and only differs in the length of time that the maximum lightness number value is requested. Note that all control profiles start from a β-value of 0, the lower limit on the lightness number. This is due to the fact that the LQR requests a rather large negative lightness number at the start.

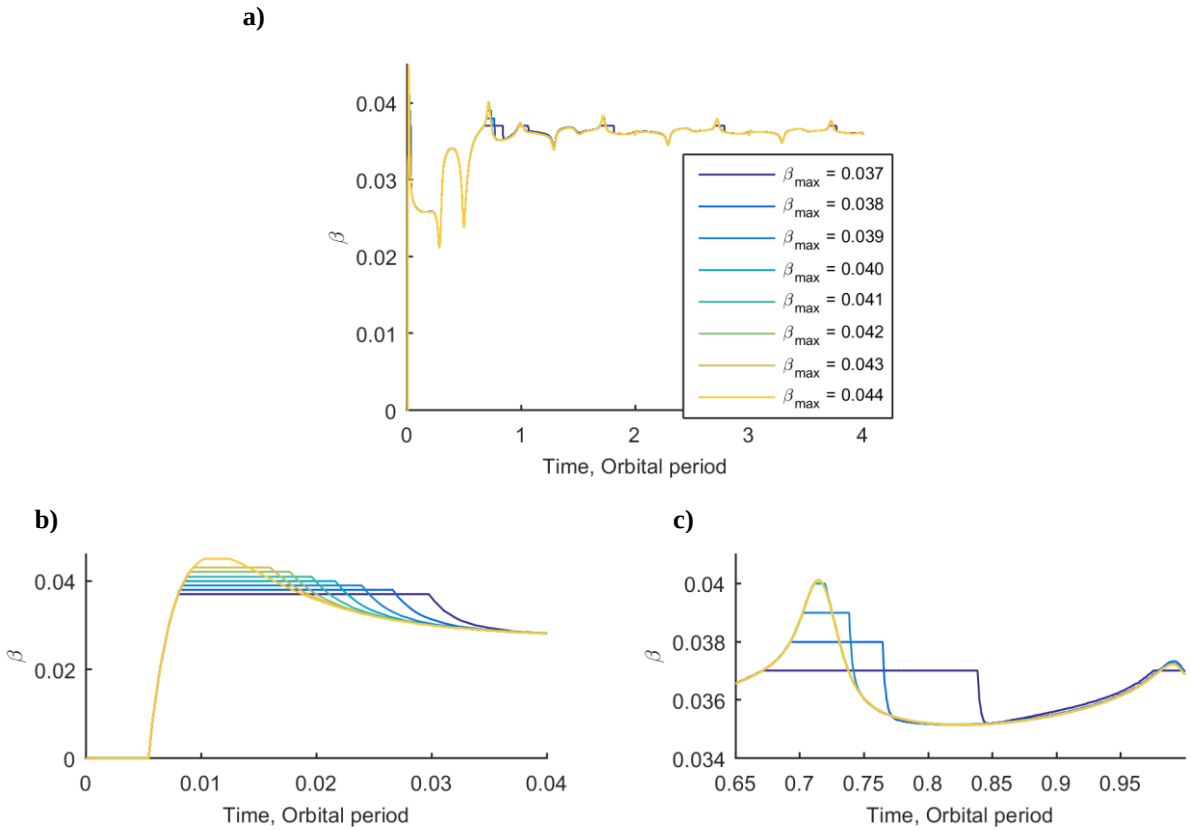

Figure 10 Orbital control of solar sail halo orbit with β = 0.0363 and Δr_0 = -800,000 km and $\Delta \dot{r}_0$ = 100 m/s. Solar sail lightness number control profile for different values for β_{max}.

7.1 Additional halo orbits

The results in Figure 8 and Figure 9 have been generated for a nominal lightness number of 0.0363. This section investigates the heliogyro performance for some of the other orbits shown in Figure 5, in particular for $\beta = 0.01$, 0.02, 0.03, and 0.04. The results are provided in Figure 11, which shows (where possible) the recoverable injection error for both a flat sail (in grey) and for a heliogyro (in color), where different values for $\beta_{\max}$ are considered for the heliogyro configuration. In particular, $\beta_{\max}$ is increased with increments of 10% up to an increase of 100%, i.e. $\beta_{\max} = \left[1+\left(i/10\right)\right]\beta$ with $i = 1,2,...,10$. Note that for $\beta = 0.01$ and 0.02 and the flat sail configuration, the recoverable injection error is so small that it is not even visible on the axis scales used in Figure 11.

The results in Figure 11 show that, the larger β, the larger the recoverable injection error. This holds both for the heliogyro and the flat sail configurations. In fact, while for $\beta = 0.03$ and 0.0363 values of $\beta_{\max} = 0.033$ and 0.038 (i.e. a 10 and 5 percent increase compared to the nominal lightness number)

achieve an order of magnitude increase in the recoverable injection error for a heliogyro compared to the flat sail configuration, such an increase is not achievable for $\beta = 0.04$. I.e. the orbital control capabilities of the flat sail seem to improve faster with the value for β than that of the heliogyro. However, still, the heliogyro significantly outperforms the flat sail configuration, which is immediately clear from comparing the grey and colored surfaces in Figure 11.

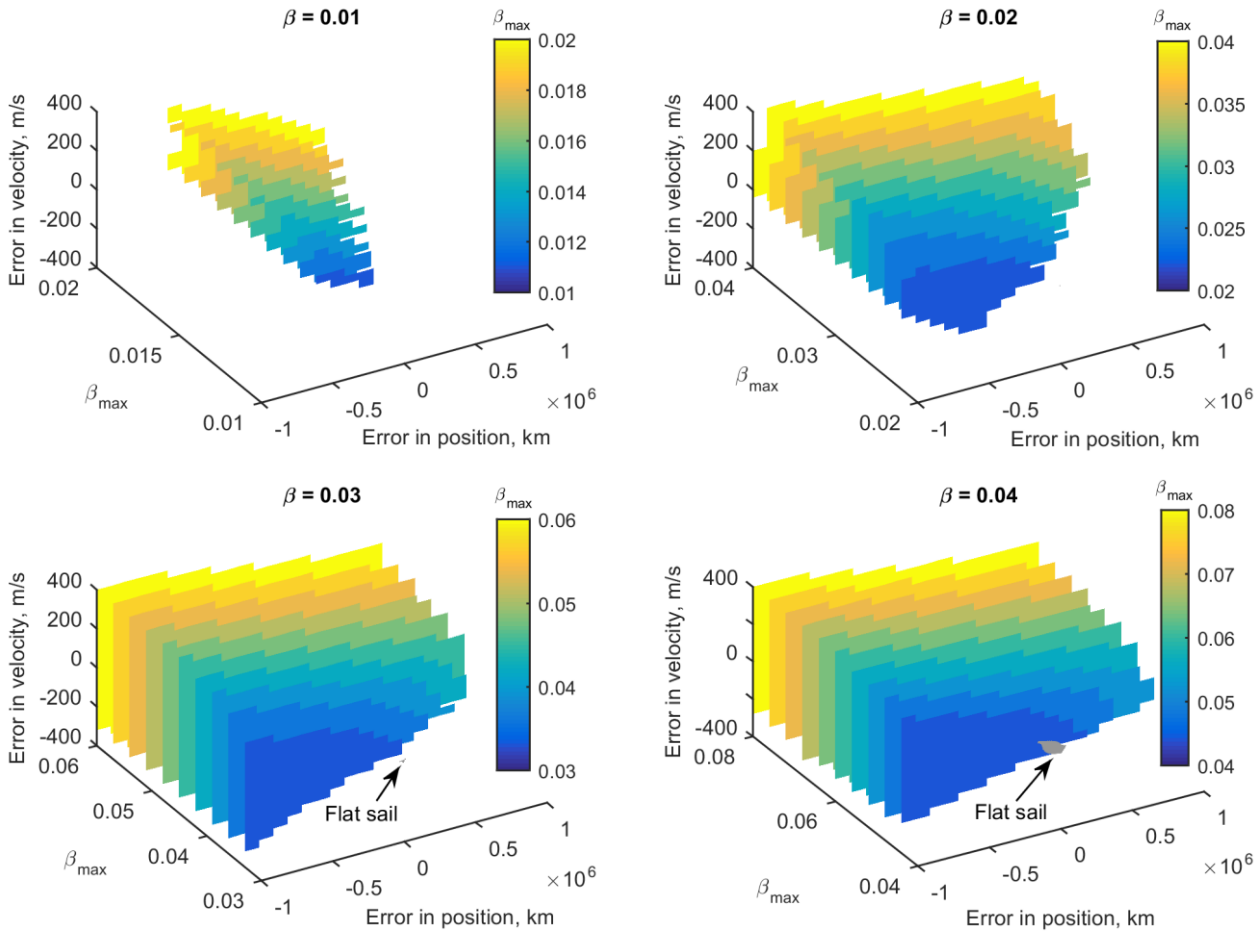

Figure 11 Orbital control of solar sail halo orbits with β = 0.01, 0.02, 0.03, and 0.04. Recoverable injection error for flat sail (in grey) and heliogyro (in color) for different values for β_{max}.

8. Sensitivity analyses

A few assumptions have been made to generate the results of Section 7, including an error tolerance of $\varepsilon = 0.0005$ and that injection into the solar sail halo orbit takes place at $y = 0$ and $z > 0$, i.e. at the northernmost point of the orbit. In this section, these parameters are varied and their effect on the orbital

control capabilities of the heliogyro are investigated. Note that, to limit the amount of results to be presented, only the case of $\beta = 0.0363$ with $\beta_{\max} = 0.04$ is considered.

8.1 Error tolerance

As mentioned, the results throughout this paper have considered the orbital control successful if, after four orbital periods, the error on position and velocity is smaller than a certain tolerance, $\varepsilon = 0.0005$, which corresponds to an allowable error in position and velocity of 75,000 km and 15 m/s, respectively. When plotting the actual errors in position and velocity after four orbital periods corresponding to Figure 8b, the results as shown in Figure 12 are obtained. Note that for computational speed, propagation is truncated when the error on the position becomes larger than 0.01 (i.e. 1,500,000 km), which is considered an unrecoverable error. The error in position in Figure 12a therefore never exceeds a value of 0.01.

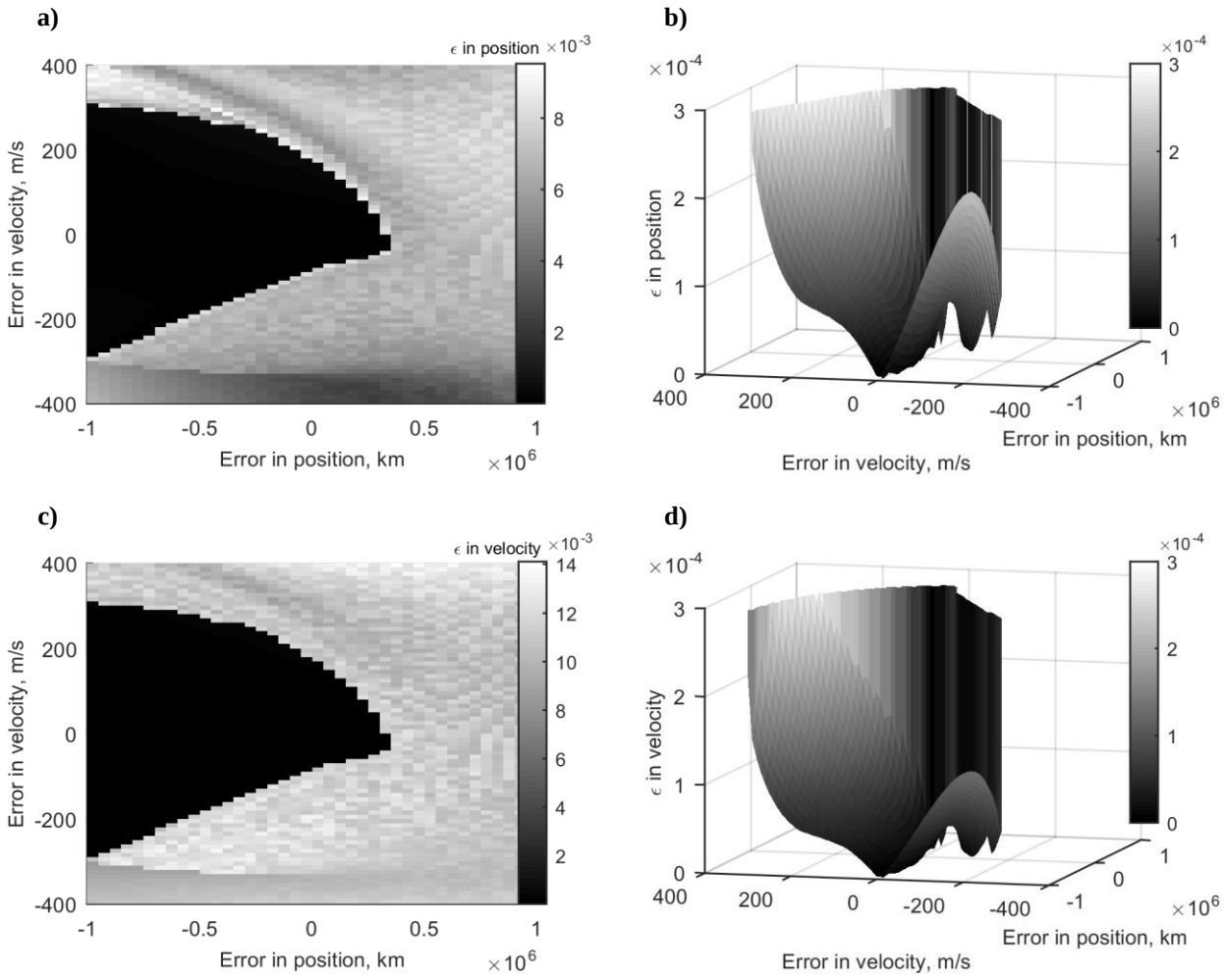

Figure 12 Orbital control of solar sail halo orbit with β = 0.0363 and β_{max} = 0.04. Achievable error tolerance, ε, on (a-b) position and (c-d) velocity after 4 orbital period.

Figure 12a and c show a very clear and sharp drop in the error on the final position and velocity between the dark grey regions ($\varepsilon < 0.001$) and the bright regions. When zooming in on the darker regions, more details appear, see Figure 12b and d. These plots show that for an error tolerance on the position of $\varepsilon \leq 0.0001$ a small region exists where this tolerance cannot be met. Something similar holds for the error in velocity, although this region exists at even smaller values for the tolerance. These regions cause the gaps in the recoverable injection error as shown in Figure 9 for $\beta_{\max} = 0.037$ as well as in Figure 13.

Figure 13 shows the recoverable injection error for the case considered in this section (i.e. for $\beta = 0.0363$ with $\beta_{\max} = 0.04$) and for $\varepsilon = 5 \cdot 10^{-5}$, $1 \cdot 10^{-4}$, $2.5 \cdot 10^{-4}$, $5 \cdot 10^{-4}$, $7.5 \cdot 10^{-4}$, and $1 \cdot 10^{-3}$. Figure 13 thus shows "horizontal slices" of the three-dimensional plots in Figure 12b and d. For larger values of the error tolerance the recoverable injection errors appear to be the same and coincide with the dark regions in Figure 12a and c. However, for small values of the error tolerance, the range of recoverable injection errors becomes smaller and the "gaps" due to the unmet tolerance on the position error (and for even smaller values also the unmet tolerance on the velocity error) become clearly visible. Although these gaps indicate that the tolerance cannot be met within 4 orbital revolutions, additional simulations have shown that the gaps reduce for longer propagation times, indicating that, given time, the gaps may disappear altogether.

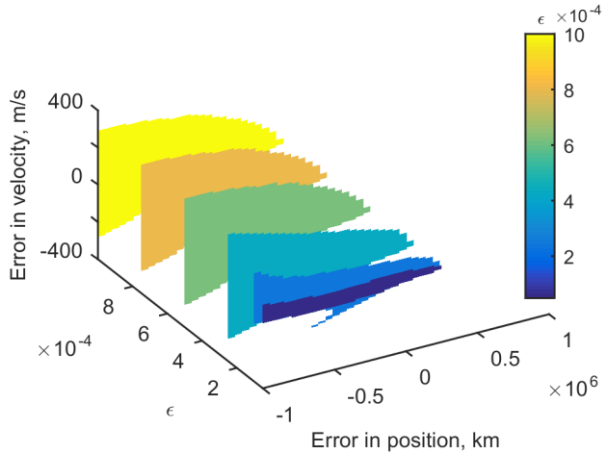

Figure 13 Orbital control of solar sail halo orbit with $\beta = 0.0363$ and $\beta_{\max} = 0.04$. Recoverable injection error for different values for the error tolerance, ε.

8.2 Injection location

The results in this paper thus far have only considered orbit injection at the most northern location of the solar sail halo orbit; however, injection may occur at any location along the orbit. In this section, four

injection locations, coinciding with the crossings of the (x,z) - and (x,y) -planes, are therefore considered (see Figure 14).

$$\mathbf{r}_0 \rightarrow \begin{cases} y=0,\ z>0 & \text{North} \\ z=0,\ y>0 & \text{East} \\ y=0,\ z<0 & \text{South} \\ z=0,\ y<0 & \text{West} \end{cases} \tag{22}$$

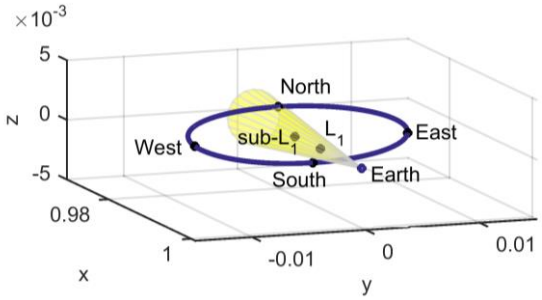

Figure 14 Alternative injection locations along the solar sail halo orbit with β = 0.0363.

The results are provided in Figure 15a and show only a minor effect of the injection location on the recoverable injection error. Only at the extremes of the position and velocity error intervals some differences can be observed, which are more clearly visible in the contour plot of Figure 15b.

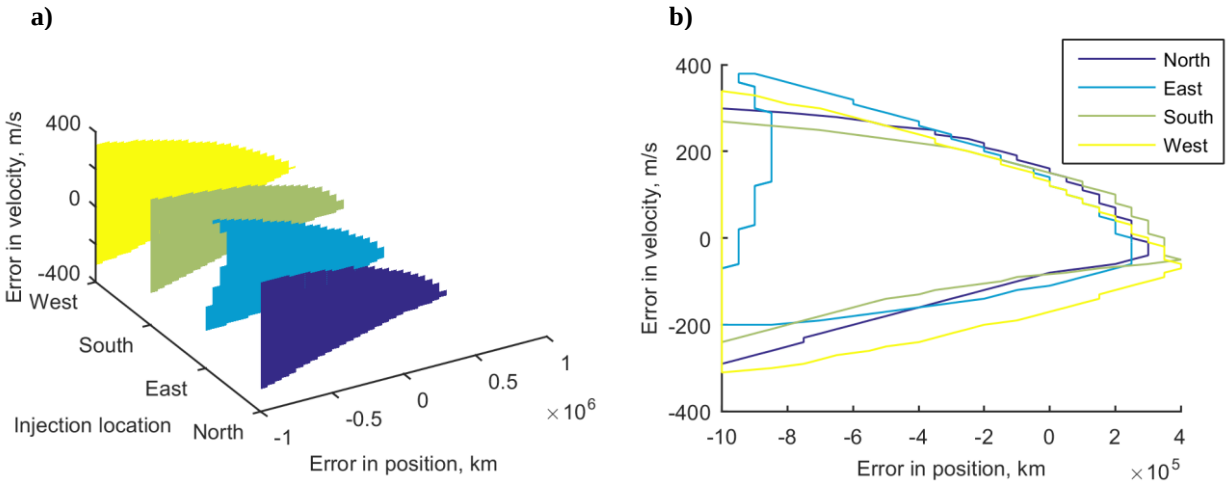

Figure 15 Orbital control of solar sail halo orbit with β = 0.0363 and β_{max}= 0.04. Recoverable injection error for different injection locations.

9. Conclusions

This paper has demonstrated the superior capabilities of a heliogyro for orbital control compared to the traditional flat sail configuration. These capabilities exist due to the heliogyro's unique ability to scale the solar sail force vector in any direction between zero and the force magnitude that an equivalent-area flat sail can generate in that direction. In other words, the heliogyro fills the well-known solar sail force-bubble and can be considered as having a highly-variable lightness number. This variable lightness number complements the sail's attitude as control variables in a linear-quadratic regulator that has been used in this paper to recover from an error in the injection state vector of a Sun-Earth L_1 solar sail halo orbit. Furthermore, the variable lightness number, as well as the smaller sail loading of a heliogyro, enables the use of a maximum lightness number that is larger than the nominal lightness number for which the solar sail halo orbit is designed. After recovering from the injection error, the heliogyro can scale down the lightness number and settle it around the nominal value.

For a solar sail halo orbit with a nominal sail lightness number of $\beta = 0.0363$ (technology designed for the Sunjammer mission) and a maximum sail lightness number of $\beta_{\max} = 0.038$ (an increase in the nominal value of 5%), the heliogyro can accommodate an order of magnitude larger range on the injection error than a flat solar sail, which has a fixed lightness number equal to the nominal value. Note that the injection error is applied in the direction of the unstable eigenvector and that control is considered successful if the error on the position and velocity after four orbital periods is smaller than a certain tolerance. If the value for $\beta_{\max}$ is increased further, an even larger injection error can be recovered with very similar β-control profiles: only the amount of time that the maximum lightness number is requested by the controller reduces with increasing $\beta_{\max}$.

For solar sail halo orbits with smaller or larger nominal sail lightness numbers, the recoverable injection error also scale down or up, respectively. This holds both for the heliogyro as for the flat sail configuration, but the heliogyro always outperforms the flat sail.

Finally, sensitivity analyses have shown that the range of recoverable injection errors does not change much within an error tolerance in the range of $1\cdot10^{-4}$ - $1\cdot10^{-3}$ (i.e. an error in position and velocity of 15,000 – 150,000 km and 3-30 m/s after 4 orbital periods). However, below a value of $1\cdot10^{-4}$, the recoverable injection errors (especially in position) do become smaller, but are still significantly larger than those recoverable with a flat sail. Also, larger injection errors for small tolerances can be overcome if propagation time is increased. Furthermore, from considering different injection locations along the orbit, it appears that the injection location has only a minor effect on the heliogyro's performance to correct for injection errors.

10. Acknowledgements

This work was funded by a John Moyes Lessells Travel Scholarship of the Royal Society of Edinburgh and by the Marie Skłodowska-Curie Individual Fellowship 658645 - S4ILS: Solar Sailing for Space Situational Awareness in the Lunar System.

11. References

[1] Tsuda, Y., Mori, O., Funase, R., Sawada, H., Yamamoto, T., Saiki, T., Endo, T., Yonekura, K., Hoshino, H., and Kawahuchi, J. *Achievement of IKAROS - Japanese Deep Space Solar Sail Demonstration Mission*, Acta Astronautica Vol. 82, 2013, pp. 183-188. DOI: 10.1016/j.actaastro.2012.03.032

[2] Johnson, L., Whorton, M., Heaton, A., Pinson, R., Laue, G., and Adams, C. *NanoSail-D: A Solar Sail Demonstration Mission*, Acta Astronautica Vol. 68, 2011, pp. 571-575. DOI: 10.1016/j.actaastro.2010.02.008

[3] Wilkie, W.K., Warren, J.E., et al., *Heliogyro Solar Sail Research at NASA*, Advances in Solar Sailing, Springer Praxis Books - Astronautical Engineering, pp. 631-650, DOI: 10.1007/978-3-642-34907-2_39

[4] McInnes, C. R., *Solar Sailing: Technology, Dynamics and Mission Applications*. Berlin: Springer-Praxis Books in Astronautical Engineering, Springer-Verlag, 1999.

[5] Guerrant, D., and Lawrence, D., *Nonlinear Torsional Dynamics and Control of Heliogyro Solar Sail Blades*, 2nd AIAA Spacecraft Structures Conference, Reston, Virginia, 2015, AIAA 2015-0435.

[6] Guerrant, D., and Lawrence, D., *Tactics for Heliogyro Solar Sail Attitude Control Via Blade Pitching*, Journal of Guidance, Control, and Dynamics, In Press. DOI: 10.2514/1.G000861

[7] West, J.L., *The Geostrom Warning Mission: Enhanced Opportunities Based on New Technology*,14th AAS/AIAA Space Flight Mechanics Conference, Maui, Hawaii, 2004, AAS 04-102.

[8] Heiligers, J., Diedrich, B., Derbes, B., and McInnes, C.R., *Sunjammer: Preliminary End-to-End Mission Design*, AIAA/AAS Astrodynamics Specialist Conference, San Diego, California, 2014, AIAA 2014-4127.

[9] Macdonald, M., and McInnes, C., *Solar Sail Mission Applications and Advancement*, Advances in Space Research, Vol. 48, No. 11, 2011, pp. 1702-1716. DOI: 10.1016/j.asr.2011.03.018

[10] Guerrant, D., and Lawrence, D., *Heliogyro Attitude Control Moment Authority via Blade Pitch Maneuvers*, Advances in Solar Sailing, Springer Praxis Books, 2014. DOI: 10.1007/978-3-642-34907-2_41

[11] Goddard Space Flight Center, Advanced Composition Explorer ACE - Detailed Mission Requirements (Report number GSFC-410-ACE-017), 1995.

[12] Nuss, J.S., *The Use of Solar Sails in the Circular Restricted Problem of Three Bodies,* MSc Thesis, Purdue University, 1998.

[13] McInnes, A.I.S., *Strategies for Solar Sail Mission Design in the Circular Restricted Three-Body Problem*, MSc Thesis, Purdue University, 2000.

[14] Baoyin, H., and McInnes, C., *Solar Sail Halo Orbits at the Sun-Earth Artificial L1-point,* Celestial Mechanics and Dynamical Astronomy, Vol. 94, No. 2, 2006, pp. 155-171. DOI: 10.1007/s10569-005-4626-3

[15] Wawrzyniak, G.G., and Howel, K.C., *Numerical Techniques for Generating and Refining Solar Sail Trajectories*, Advances in Space Research, Vol. 48, No. 11, 2011, pp. 1848-1857. DOI: 10.1016/j.asr.2011.04.012

[16] Waters, T.J., and McInnes, C.R., *Periodic Orbits Above the Ecliptic in the Solar-Sail Restricted Three-Body Problem*, Journal of Guidance, Control, and Dynamics, Vol. 30, No. 3, 2007, pp. 687-693. DOI: 10.2514/1.26232

[17] Heiligers, J., Hiddink, S., Noomen, R., and McInnes, C., *Solar Sail Lyapunov and Halo Orbits in the Earth-Moon Three-Body Problem,* Acta Astronautica, Vol. 116, 2015, pp. 25-35. DOI: 10.1016/j.actaastro.2015.05.034

[18] Ceriotti, M., and McInnes, C.R., *Hybrid Solar Sail and SEP Propulsion for Novel Earth Observation Missions*, 61st International Astronautical Congress, Prague, Czech Republic, 2010.

[19] Heiligers, J., Ceriotti, M., McInnes, C.R., and Biggs, J.D., *Design of Optimal Transfers Between North and South Pole-sitter Orbits*, 22nd AAS/AIAA Space Flight Mechanics Meeting, Charleston, South Carolina, 2012, AAS 12-164.

[20] Ceriotti, M., Heiligers, J., and McInnes, C.R., *Trajectory and Spacecraft Design for a Pole-Sitter Mission,* Journal of Spacecraft and Rockets, Vol. 51, No. 1, 2014, pp. 311-326. DOI: 10.2514/1.A32477

Appendix A Reference frames and transformations

Following Reference 10, four different reference frames are involved in defining the forces and moments produced by a heliogyro, see Figure 16. (Note that there is a slight difference in the definition of the $D\left(\hat{\mathbf{d}}_1,\hat{\mathbf{d}}_2,\hat{\mathbf{d}}_3\right)$-frame with Reference 10).

1. Sun coordinate system, $S\left(\hat{\mathbf{s}},\hat{\mathbf{l}},\hat{\mathbf{p}}\right)$
   - $\hat{\mathbf{s}}$: Sun-spacecraft vector (for heliocentric orbits $\hat{\mathbf{s}} \| \hat{\mathbf{r}}$), referred to as 'radial'

- $\hat{\mathbf{l}}$: Local horizontal with respect to the Sun (for heliocentric orbits $\hat{\mathbf{l}} \| \hat{\mathbf{v}}$), referred to as 'transverse'
- $\hat{\mathbf{p}}$: Reference axis for the clock angle δ (for heliocentric orbits $\hat{\mathbf{p}} \| \hat{\mathbf{h}}$)

2. Despun coordinate system, $D\left(\hat{\mathbf{d}}_1, \hat{\mathbf{d}}_2, \hat{\mathbf{d}}_3\right)$
   - $\hat{\mathbf{d}}_1$: Along the heliogyro spin axis $\boldsymbol{\Omega}$
   - $\hat{\mathbf{d}}_2$: Completes the right handed reference frame (along blade 4 at time $t = 0$)
   - $\hat{\mathbf{d}}_3$: Along blade 1 at time $t = 0$

   This reference frame is thus defined at time $t = 0$ and remains fixed while the heliogyro rotates.

3. Body coordinate system, $B\left(\hat{\mathbf{b}}_1, \hat{\mathbf{b}}_2, \hat{\mathbf{b}}_3\right)$
   - $\hat{\mathbf{b}}_1$: Along blade 1 at time t
   - $\hat{\mathbf{b}}_2$: Completes right handed reference frame (along blade 4 at time t)
   - $\hat{\mathbf{b}}_3$: Along the heliogyro spin axis $\boldsymbol{\Omega}$

   This reference frame is thus fixed to the blades and rotates while the heliogyro rotates.

4. Flat i^{th} blade coordinate system, $L_i\left(\hat{\mathbf{x}}, \hat{\mathbf{y}}, \hat{\mathbf{z}}\right)$
   - $\hat{\mathbf{x}}$: Along i^{th} blade span
   - $\hat{\mathbf{y}}$: Along i^{th} blade chord
   - $\hat{\mathbf{z}}$: Normal to i^{th} blade ($\hat{\mathbf{z}} \| \hat{\mathbf{n}}$)

To transform between these reference frames, the following rotation operations are required, where the following definition and notation of the standard rotation matrices is adopted:

$$R_{x,\gamma} = \begin{bmatrix} 1 & 0 & 0 \\ 0 & \cos\gamma & -\sin\gamma \\ 0 & \sin\gamma & \cos\gamma \end{bmatrix}, \; R_{y,\gamma} = \begin{bmatrix} \cos\gamma & 0 & \sin\gamma \\ 0 & 1 & 0 \\ -\sin\gamma & 0 & \cos\gamma \end{bmatrix}, \; R_{z,\gamma} = \begin{bmatrix} \cos\gamma & -\sin\gamma & 0 \\ \sin\gamma & \cos\gamma & 0 \\ 0 & 0 & 1 \end{bmatrix} \tag{23}$$

1. Transformation from $D\left(\hat{\mathbf{d}}_1, \hat{\mathbf{d}}_2, \hat{\mathbf{d}}_3\right) \rightarrow S\left(\hat{\mathbf{s}}, \hat{\mathbf{l}}, \hat{\mathbf{p}}\right)$

   A vector in, $D\left(\hat{\mathbf{d}}_1, \hat{\mathbf{d}}_2, \hat{\mathbf{d}}_3\right)$, $\mathbf{x}_D$, can be transformed to a vector in $S\left(\hat{\mathbf{s}}, \hat{\mathbf{l}}, \hat{\mathbf{p}}\right)$, $\mathbf{x}_S$, through

$$\mathbf{x}_S = R_{z,\alpha} R_{x,\delta} \mathbf{x}_D = [SD] \mathbf{x}_D \tag{24}$$

2. Transformation from $B\left(\hat{\mathbf{b}}_1, \hat{\mathbf{b}}_2, \hat{\mathbf{b}}_3\right) \rightarrow D\left(\hat{\mathbf{d}}_1, \hat{\mathbf{d}}_2, \hat{\mathbf{d}}_3\right)$

   A vector in $B\left(\hat{\mathbf{b}}_1, \hat{\mathbf{b}}_2, \hat{\mathbf{b}}_3\right)$, $\mathbf{x}_B$, can be transformed to a vector in $D\left(\hat{\mathbf{d}}_1, \hat{\mathbf{d}}_2, \hat{\mathbf{d}}_3\right)$, $\mathbf{x}_D$, through

$$\mathbf{x}_D = R_{y,-\frac{\pi}{2}} R_{x,\pi} R_{z,\psi_1} \mathbf{x}_B = \left[DB\right]\mathbf{x}_B, \tag{25}$$

where ψ_i is defined as

$$\psi_i = \Omega t + \chi_i, \quad \chi_i = 2\pi \frac{i-1}{N}, \tag{26}$$

with i the i^{th} blade number and N the number of heliogyro blades. The constant π and $-\pi/2$ rotations are merely to change the axis numbering to align with convention in literature.

3. Transformation from $L_i\left(\hat{\mathbf{x}},\hat{\mathbf{y}},\hat{\mathbf{z}}\right) \rightarrow B\left(\hat{\mathbf{b}}_1,\hat{\mathbf{b}}_2,\hat{\mathbf{b}}_3\right)$

A vector in $L_i\left(\hat{\mathbf{x}},\hat{\mathbf{y}},\hat{\mathbf{z}}\right)$, $\mathbf{x}_{L_i}$, can be transformed to a vector in $B\left(\hat{\mathbf{b}}_1,\hat{\mathbf{b}}_2,\hat{\mathbf{b}}_3\right)$, $\mathbf{x}_B$, through

$$\mathbf{x}_B = R_{z,-\chi_i} R_{x,\theta_i} \mathbf{x}_{L_i} = \left[BL_i\right]\mathbf{x}_{L_i}, \tag{27}$$

with θ_i the pitch angle of the blade.

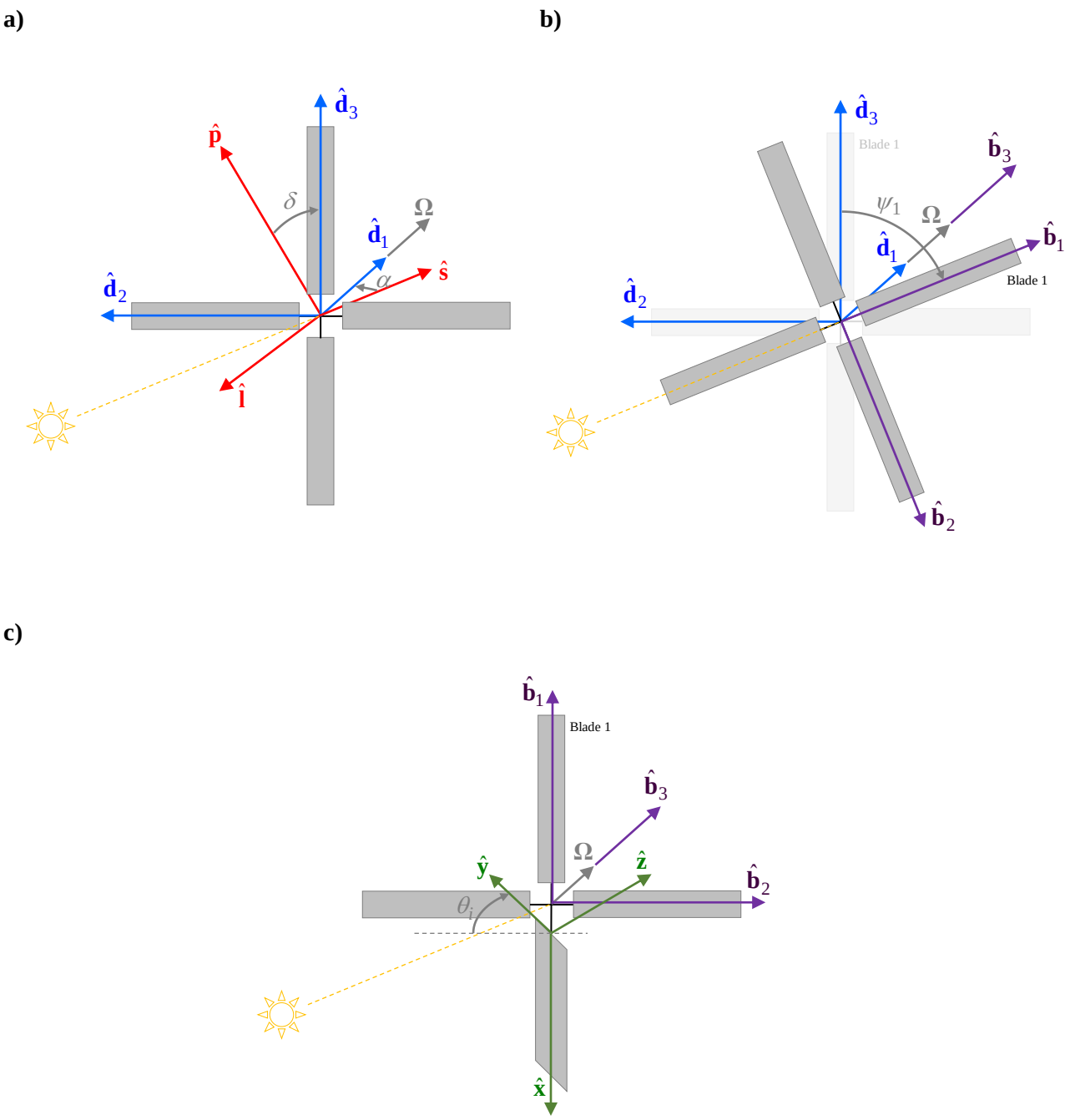

Figure 16 Reference frames involved in the computation of forces and moments on heliogyro.

a) S **- and** D **-frames. b)** D **- and** B **-frames. c)** B **- and** L_i **-frames.**